

# Blade Element Momentum Modeling of Low-Reynolds Electric Propulsion Systems

Matthew H. McCrink\* and James W. Gregory†  
The Ohio State University, Columbus, Ohio 43235

DOI: 10.2514/1.C033622

A model for the propulsion system of a small-scale electric unmanned aerial system is presented. This model is based on a blade element momentum (BEM) model of the propeller, with corrections for tip losses, Mach effects, three-dimensional flow components, and Reynolds scaling. Particular focus is placed on the estimation of scale effects not commonly encountered in the full-scale application of the BEM modeling method. Performance predictions are presented for geometries representative of several commercially available propellers. These predictions are then compared with experimental wind tunnel measurements of the propellers' performance. The experimental data support the predictions of the proposed BEM model and point to the importance of scale effects on prediction of the overall system performance.

## Nomenclature

$A$	=	test section area, $m^2$
$a_0$	=	axial inflow correction factor
$a_1$	=	radial inflow correction factor
$B$	=	number of blades
$C$	=	faring area, $m^2$
$C_d$	=	drag coefficient
$C_l$	=	lift coefficient
$C_{l,pot}$	=	lift coefficient from potential flow theory
$C_n$	=	normal force coefficient
$C_P$	=	power coefficient
$C_Q$	=	torque coefficient
$C_T$	=	thrust coefficient
$c$	=	chord, m
$D$	=	diameter, m
$dr$	=	differential radial blade element, m
$E$	=	voltage, V
$F$	=	Prandtl tip loss correction factor
$f$	=	local Prandtl tip loss correction factor
$I$	=	current, A
$J$	=	advance ratio
$K$	=	local velocity correction factor
$L/D$	=	lift-to-drag ratio
$M$	=	Mach number
$n$	=	rotation rate, rev/s
$P$	=	power, W
$Q$	=	torque, $N \cdot m$
$q$	=	dynamic pressure, Pa
$R$	=	propeller radius, m
$Re$	=	Reynolds number
$r$	=	radial position, m
$T$	=	thrust, N

$\mathcal{V}$	=	fairing volume, $m^3$
$V$	=	velocity, m/s
$V_l$	=	local section velocity, m/s
$V_r$	=	radial velocity, m/s
$V_\infty$	=	freestream velocity, m/s
$V_1$	=	velocity across propeller disk, m/s
$V_2$	=	downstream velocity, m/s

## Greek

$\alpha$	=	angle of attack, rad
$\eta_{\text{electrical}}$	=	electrical efficiency
$\eta_{\text{propulsive}}$	=	propulsive efficiency
$\eta_{\text{total}}$	=	total system efficiency
$\eta$	=	efficiency
$\theta$	=	geometric angle of attack, rad
$\phi$	=	Inflow angle, rad
$\rho$	=	density, $kg/m^3$
$\sigma$	=	propeller solidity
$\tau$	=	tunnel correction factor
$\mu$	=	viscosity, $kg/(m \cdot s)$
$\omega$	=	rotation rate, rad/s

## I. Introduction

DEVELOPMENT of a predictive propulsion model for small-scale unmanned aerial systems (sUAS) represents a continuing challenge for the designers of these vehicles. Typical components available for sUAS are not supported by robust performance data sets. This paper presents a predictive performance model for an electric propulsion system typical of sUAS. The model attempts to capture the effects of Reynolds scaling on the overall performance of the system at various operating conditions. The predictive model is based on the blade element momentum (BEM) methodology, which has been widely used for full-scale wind turbines, helicopters, and propellers [1–5]. Several corrections to the basic model are needed in order to capture the effects of compressibility, viscosity, and three-dimensional (3D) flows, and are presented in Sec. II.A.

The BEM modeling methodology has been applied to small-scale propeller testing by Uhlig and Selig [4] to predict the performance at extreme angles of attack, but without handling Reynolds scaling effects. Ol et al. [6] presented BEM predictions for a small-scale propeller with experimental data, demonstrating the large impact of geometry estimation errors on the resulting propulsive performance. No specific BEM correction factors were mentioned in these works. Several investigations report experimental data sets for sUAS propellers [7–9], and acknowledge the lack of published performance information. The systematic development of a scale-specific model with experimental validation for small-scale propeller and propulsion system performance is still lacking.

Presented as Paper 2015-3296 at the 33rd AIAA Applied Aerodynamics Conference, Dallas, TX, 22–26 June 2015; received 6 July 2015; revision received 18 March 2016; accepted for publication 23 March 2016; published online 19 July 2016. Copyright © 2016 by Matthew H. McCrink and James W. Gregory. Published by the American Institute of Aeronautics and Astronautics, Inc., with permission. Copies of this paper may be made for personal and internal use, on condition that the copier pay the per-copy fee to the Copyright Clearance Center (CCC). All requests for copying and permission to reprint should be submitted to CCC at [www.copyright.com](http://www.copyright.com); employ the ISSN 0021-8669 (print) or 1533-3868 (online) to initiate your request.

\*Postdoctoral Researcher, Department of Mechanical and Aerospace Engineering, Aerospace Research Center, 2300 West Case Rd. Member AIAA.

†Associate Professor, Department of Mechanical and Aerospace Engineering, Aerospace Research Center, 2300 West Case Rd. Associate Fellow AIAA.

The variation in performance over a range of Reynolds numbers was measured by Brandt and Selig [7]. In their work, the propeller RPM was held constant and the efficiency versus advance ratio was measured. As the Reynolds number was reduced, the overall propulsive efficiency decreased. Brandt and Selig concluded that there are significant Reynolds-based effects on small propellers that are not typically encountered on large-scale, higher-power propellers. Merchant and Miller measured the reduction in propulsive efficiency at different local Reynolds numbers for different sUAS propellers [10]. In their work, the reduction in propulsive efficiency was tied to the reduction in lift, and increase in drag at low Reynolds numbers. In a similar manner, Ol et al. also measured a reduction in propulsive efficiency at low Reynolds numbers [6]. In all reported cases, the Reynolds number effects were measured by holding the propeller RPM constant as the advance ratio was increased. A reduction in local Reynolds number typically results in a decreased  $L/D$  for a given angle of attack. The reduced  $L/D$  translates to lower thrust for a similar power input. The lift and drag variation of immersed lifting surfaces at low Reynolds numbers has been well documented in various works [11–14].

This work seeks to match the performance predictions of a BEM model to experimental data gathered on geometrically similar propellers over a range of Reynolds numbers. Emphasis is placed on the quantification of operational conditions and local Reynolds number effects on the overall propulsive efficiency. Reynolds effects are anticipated to be of first-order importance to the propeller performance, yet no BEM models applied to small-scale propellers have substantiated this hypothesis. Thus, carefully controlled experiments were conducted in order to produce constant Reynolds number propeller data across a range of test conditions. A key contribution of this work is the incorporation of Reynolds effects in the BEM model, and experimental demonstration of the first-order importance of these effects when modeling small-scale propellers.

Experimental extensions to the model include capturing the electrical efficiency of the system. This will allow estimates of the electrical efficiency to be combined with the propeller efficiency, yielding a model relating the measured electrical power to the thrust power. The BEM model can be used along with real-time measurements of airspeed, propeller rotation speed, and electrical power to infer the power supplied to the flow under various flight test conditions. This estimate is valuable for rapid flight test determination of the aircraft drag polar and closed-loop control for real-time optimization of vehicle performance. This method of in-flight determination of power is necessary for production aircraft that are typically not instrumented with load cells that can directly measure thrust and torque. The BEM model developed here is also valuable for propeller and aircraft design, because it enables rapid iteration on relevant design variables with accurate results.

## II. Blade Element Momentum Model

### A. Modeling Overview

The BEM model attempts to incorporate the geometric properties of the propeller system into a momentum-transfer-based model of the flow. Determination of the thrust production and torque required derives from individually analyzing small elemental sections along the span. In this work, data on elemental sections are generated computationally, creating a look-up table for input to the BEM model. The individual forces acting on each section are integrated to find the total force in the direction of motion, the thrust, and the torque opposing the rotation of the blade. Figure 1 shows the streamtube encapsulating the propeller, and Fig. 2 shows the basic forces acting on an elemental blade section.

The differential force and torque components are integrated over the surface of the blade to determine the total force and torque produced by the propeller. A detailed derivation of the BEM model can be found in [1]. A basic overview of the BEM model as it applies to the current construct is presented here. The primary difficulty in BEM modeling is the estimation of the induced axial and radial velocity components created by the rotating propeller. As the propeller is operating in a predominantly subsonic regime, the

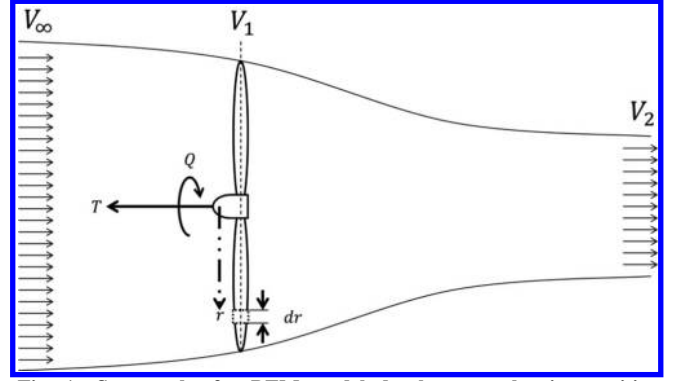


Fig. 1 Streamtube for BEM model development showing positive elemental propeller force and torque conventions.

pressure field created by the propeller induces a rotational flow component upstream of the blade. The magnitude and direction of the induced velocity components vary in the spanwise direction as a function of the propeller aerodynamic, geometric, and operational conditions. To date, there is no closed form solution for the induction factors. Therefore, an iterative approach is used to approximate them over a finite section of the propeller blade. The induced velocity factors,  $a_0$  and  $a_1$ , are formulated by equating the local aerodynamic forces acting on the blade with the bulk momentum transfer of the blade to the streamtube surrounding the propeller. The thrust and torque components acting on each blade element are given by [1]

$$\begin{aligned} dT &= \frac{1}{2} \rho V_\infty^2 c B \frac{(1 + a_0)^2}{\sin^2 \phi} C_T dr \\ dQ &= \frac{1}{2} \rho V_\infty c B \omega r^2 \frac{(1 + a_0)(1 - a_1)}{\sin \phi \cos \phi} C_Q dr \end{aligned} \quad (1)$$

where  $C_T$  and  $C_Q$  are related to the local lift and drag coefficients by the rotation matrix given as

$$\begin{bmatrix} C_T \\ C_Q \end{bmatrix} = \begin{bmatrix} \cos \phi & -\sin \phi \\ \sin \phi & \cos \phi \end{bmatrix} \begin{bmatrix} C_l \\ C_d \end{bmatrix} \quad (2)$$

and the lift and drag coefficients can be determined across a range of conditions by experimental, analytical, or computational methods.

From Fig. 1, the total thrust can be determined via momentum balance between the upstream farfield and a location far downstream (shown as location 2 in Fig. 1). Applying the conservation of momentum to the streamtube gives the following relationship for the thrust and torque components across the propeller disk:

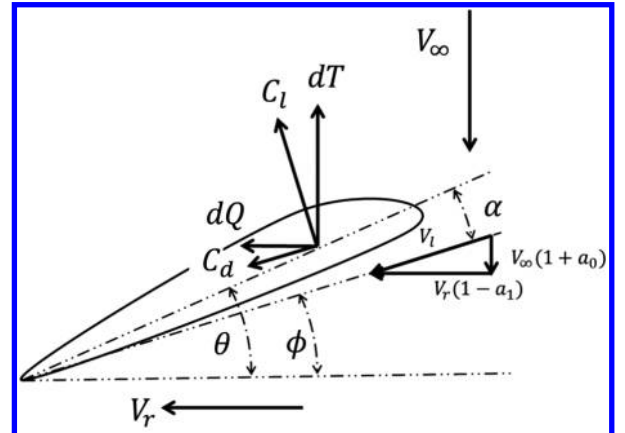


Fig. 2 Local blade section properties for BEM model development. Forces and torque represent those acting on an infinitesimal blade element.

$$\begin{aligned} dT &= 4\pi r \rho V_\infty^2 (1 + a_0) a_0 dr \\ dQ &= 4\pi r^3 \rho V_\infty \omega (1 + a_0) a_1 dr \end{aligned} \quad (3)$$

Equating Eq. (3) with the geometric thrust and torque terms in Eq. (1) gives the following implicit relationship between the induced velocity components:

$$\begin{aligned} a_0 &= \frac{1}{(4 \sin^2 \phi / \sigma C_T) - 1} \\ a_1 &= \frac{1}{(4 \sin \phi \cos \phi / \sigma C_Q) + 1} \end{aligned} \quad (4)$$

where  $\sigma$  is the local solidity of the disk, given as the ratio of the local chord divided by the area of the annular disk formed by the infinitesimal radial blade element,  $cB/2\pi r$  [15,16]. Using the relations provided by Eqs. (3) and (4), an implicit iterative solver can be set up to approximate the axial and radial induction factors.

## B. Corrections

The BEM model is nominally a two-dimensional (2D) estimation of local blade performance and therefore provides no connection between adjacent infinitesimal blade elements. For blades of moderate aspect ratio, there will be an appreciable spanwise variation in velocity, angle of attack, and Reynolds number. Under some conditions, the radial flow components can affect the propulsive efficiency of the propeller [3]. To account for the spanwise aerodynamic coupling, correction factors are introduced. These include allowances for tip losses, Mach effects, and pressure-based radial flow components. The following sections detail these corrections.

### 1. Tip Loss Factor

Because of pressure equalization, the lift goes to zero as the radial location approaches the tip. Prandtl addressed this effect by incorporation of a tip loss coefficient [17]. The tip loss factor is given as

$$F = \left(\frac{2}{\pi}\right) \cos^{-1}(e^{-f}) \quad (5)$$

and the localized correction factor  $f$  is given by

$$f = \frac{B}{2} \left( \frac{1-r}{r\phi} \right) \quad (6)$$

where  $B$  is the number of blades and  $\phi$  is the local inflow angle ( $\theta - \alpha$ ). Because the inflow angle is not known a priori, it must be determined iteratively in the BEM algorithm. These corrections represent a reduction in lift occurring near the tip of a blade element because of pressure equalization. The tip loss coefficient is incorporated into the BEM model by modifying the inflow coefficients  $a_0$  and  $a_1$  [16]:

$$\begin{aligned} a_0 &= \frac{1}{(F4 \sin^2 \phi / \sigma C_T) - 1} \\ a_1 &= \frac{1}{(F4 \sin \phi \cos \phi / \sigma C_Q) + 1} \end{aligned} \quad (7)$$

### 2. Mach Number Correction

The tip Mach number on low-pitch propellers can reach up to 0.6. At these Mach numbers, the 2D airfoil sections will experience an increase in the lift curve slope approximated by Glauert's Mach correction factor, [15] given as

$$C_l = \frac{C_{l,M=0}}{\sqrt{1-M^2}} \quad (8)$$

The Mach correction is applied to the lift coefficient and drag coefficient for the cases considered in this work.

### 3. Three-Dimensional Flow Correction

BEM theory fundamentally assumes quasi-2D flow, with no interaction between adjacent radial locations. However, spanwise flows are often present and cannot be accounted for with the baseline BEM technique. Thus, a semi-empirical correction must be used to address 3D flow effects induced by the rotation of the blade [3,18,19]. The correction model used in this work follows the work of Snel et al. [3] and Liu and Janajreh [19] and will be briefly summarized here within the context of propeller performance. The basic BEM model assumes that the blade sections are decoupled in the spanwise direction. Spanwise (radial) flows occur because of the presence of locally separated regions near the training edge that extend over some portion of the blade surface. The complex pressure field resulting from these separated regions promotes a radial flow component that tends to move from root to tip, as the spanwise pressure gradient is stronger than the chordwise gradient in these separated regions. The bulk movement of fluid requires additional energy from the motor. The additional energy is formulated similarly to a mechanical pumping loss term. Semi-empirical corrections for the "pumping" loss were proposed by Snel et al. and Liu and Janajreh after detailed theoretical, computational, and experimental investigations. The correction relies on modification of the local lift coefficient based on its angle of attack and proximity to other stalled blade regions.

A reduction in the radial flow component occurs near the tip as a result of a lower angle of attack and localized pressure equalization. To match the extents of the 3D effects, the centrifugal pumping correction is applied between the root and 85% of the span [3]. The semi-empirical 3D correction is formulated by augmenting the uncorrected 2D normal force components, given by

$$C_{n_{3-D}} = C_{n_{2-D}} + 1.5 \left( \frac{c}{r} \right)^2 (C_{l_{\text{pot}}} - C_{l_{2-D}}) \left( \frac{\omega r}{V_l} \right)^2 \quad (9)$$

where the normal force coefficient is normal to the local airfoil chord.  $C_{l_{\text{pot}}}$  is the lift coefficient from thin airfoil theory (potential flow) for a symmetric section evaluated at the local angle of attack. Estimation of the aerodynamic parameters required for the BEM model and correction factors are addressed in the following sections. The results from the BEM model will be compared with the experimental measurements detailed in the next section.

## III. BEM Model and Experimental Parameters

This section details the performance parameters used in the BEM model and experimental testing. A discussion of a visual technique used for estimation of the propeller geometry is presented. A description of the aerodynamic characteristics of the propeller blade sections is also presented.

### A. Propeller Performance Metrics

This section details the terminology and metrics associated with the analysis of the propeller-based propulsion system. These include the nondimensional parameters commonly associated with propeller design such as the advance ratio, thrust and power coefficients, and the propulsive efficiency.

The advance ratio is a dimensionless term used to quantify the effects of forward motion and angular velocity and is given as

$$J = \frac{V_\infty}{nD} \quad (10)$$

where  $J$  is the advance ratio,  $n$  is the rotational frequency in rev/s, and  $D$  is the diameter of the propeller. The thrust and power coefficients are nondimensional quantities relating the thrust and power-producing capability of a propeller to its rotational velocity and diameter. From dimensional analysis, the thrust coefficient is given as

$$C_T = \frac{T}{\rho n^2 D^4} \quad (11)$$

where  $T$  is the thrust,  $\rho$  the freestream density,  $n$  the rotation rate of the propeller, and  $D$  is the diameter. Following a similar development, the torque and power coefficients are expressed as

$$C_Q = \frac{Q}{\rho n^2 D^5}, \quad C_P = \frac{P}{\rho n^3 D^5} \quad (12)$$

where  $Q$  is the torque and  $P$  is the motor power required to drive the propeller [16].

The propulsive efficiency is given as the ratio of the power transferred to the air mass moving through the propeller disk to the mechanical power required to drive the propeller. This is expressed as

$$\eta_{\text{propulsive}} = \frac{TV_\infty}{2\pi n Q} = \frac{1}{2\pi} \frac{C_T}{C_Q} J \quad (13)$$

The propulsive efficiency is a key metric for comparison of propellers of different geometric configurations or operational conditions. For the electrical propulsion system used in this work, there is an additional electrical efficiency term used to correlate the electrical power delivered from the battery to the mechanical power produced by the motor. This efficiency term is given by

$$\eta_{\text{electrical}} = \frac{2\pi n Q}{EI} \quad (14)$$

where  $E$  is the battery voltage and  $I$  is the supplied current to the electronic speed controller. In practice, the speed controller and motor efficiencies are lumped into a single term. The total system efficiency, a ratio of flow power to supplied electrical power, is therefore the product of the electrical and propulsive efficiencies:

$$\eta_{\text{total}} = \eta_{\text{electrical}} \eta_{\text{propulsive}} \quad (15)$$

## B. Geometric and Aerodynamic Parameters

### 1. Propeller Geometry Estimation

The APC propellers used in this work are hobby-grade models commonly used on sUAS, and do not have published tolerances on the geometry. Furthermore, specific information on the variation of chord or geometric angle of attack ( $\theta$ ) across the span of the propeller is unknown. Thus, a visual integration method was developed in order to determine the blade geometry, following the method suggested by Deters et al. [14] and Ol et al. [6]. The integration method correlates two perpendicular images to estimate the spanwise variation of chord and angle of attack. A third perpendicular image is used in difficult-to-resolve regions, typically occurring near the root and tip. The specific propellers investigated with the BEM model are the APC thin electric 10 × 5E, 10 × 6E, and 10 × 7E. The first number in the nomenclature represents the diameter of the blade (in inches). The second number represents the theoretical forward advance (pitch) in one revolution of the blade (again, in inches). The propellers use the Clark Y airfoil section from 0 to 5% span, and the NACA 4412 for the remainder of the span. The airfoil distribution was determined by cutting the blades in 10% increments and imaging the cross cut sections. Ol et al. proposed a similar method in which the cross cut sections were automatically fit with splines. Their splines were then matched to airfoil data accessed through the University of Illinois at Urbana–Champaign airfoil database. In this work, a similar manual version of this method was used, where splines were fit to the cross cut sections and compared with standard NACA profiles.

For each propeller, two perpendicular images were collected. The first is in the streamwise direction allowing for identification of the hub region. The hub contains features of known sizes, which provide data for scaling and rotation. The second image is perpendicular to the streamwise direction and span. A black line was drawn on the leading edge to allow for proper edge identification. Figures 3 and 4 show representative images for each blade. The images were collected with a 10 MP Canon DSLR camera taken from 0.5 m,



Fig. 3 Top view of APC 10 × 5E, 10 × 6E, and 10 × 7E propellers, from top to bottom.



Fig. 4 Side view of APC 10 × 5E, 10 × 6E, and 10 × 7E propellers, from top to bottom. Spanwise black lines used for leading edge detection.

giving an effective resolution of 0.1 mm per pixel at a distance of 0.5 m. From these images, negatives were formed using the edge detection and correction capabilities of the GIMP image editing software package, the results of which are shown in Fig. 5. The negative images were derotated and scaled using the MATLAB image processing toolbox. Scaling relies on correlating known dimensions with pixel counts. The images taken in the streamwise direction show the hub and mounting hole, the dimensions of which were directly measured with calipers. After scaling based on hub size, the blade is derotated using a known overall length.

Alignment and registration of the top and side negatives occurs by finding the maximum cross-correlation between the top and side images. The chord is estimated by integrating the pixel count in the streamwise direction across the top image and the chordwise direction of the side image. The local chord is then the square root of the sum of the squares of the top and side lengths estimated by pixel integration. The inverse tangent of the top and side pixel integral values gives the geometric angle of attack. Figure 6 shows the resulting angle of attack and chord variation for the blades used in this work. The BEM model calculations start immediately outside the hub region. The hub is shown in Fig. 6 and included only for clarity.

The resulting propeller geometry was verified using a NextEngine 3D scanner. This system generates a precise map of 3D surfaces. However, it is unable to simultaneously map the underside of the propeller, making it unsuitable for complete definition of the propeller geometry. The accuracy of the sensor is limited to 0.5 mm with an overall point spacing of 2 mm. The results are a coarse estimate of the propeller geometry bounding the estimates provided by the imaging technique previously outlined. A representative dataset for the APC 10 × 6E is shown in Fig. 7, which confirms the validity of the imaging technique.

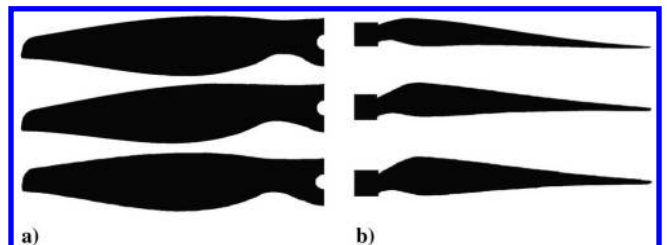


Fig. 5 APC propeller top (a) and side (b) negative images for the APC 10 × 5E, 10 × 6E, and 10 × 7E (top to bottom).



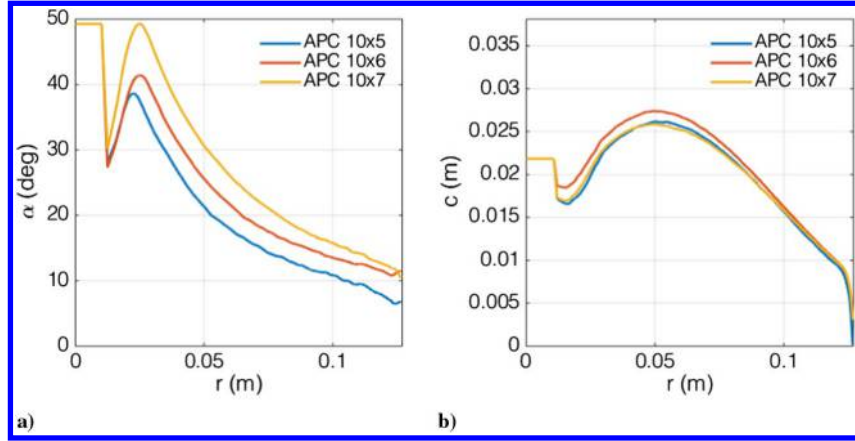


Fig. 6 Angle of attack (a) and chord length (b) for APC  $10 \times 5$ E,  $10 \times 6$ E, and  $10 \times 7$ E propellers.

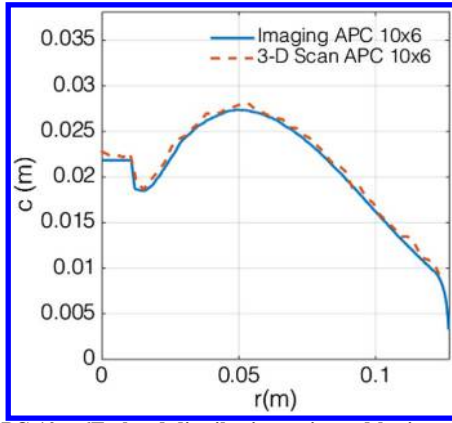


Fig. 7 APC  $10 \times 6$ E chord distribution estimated by imaging and 3D scan.

## 2. Aerodynamic Coefficients

The aerodynamic coefficients for the BEM model were generated using XFOIL and augmented with experimental data. XFOIL is a panel code designed to model the effects of viscosity (to first order), and hence Reynolds number on various aerodynamic bodies [20]. XFOIL was used to analyze 2D sections over a range of Reynolds numbers from  $10^4$  to  $10^6$ , and angles of attack from  $-10$  to  $20$  deg in  $0.5$  deg increments (see Figs. 8 and 9) at a Mach number of zero. For angles of attack beyond stall, high-angle-of-attack experimental data from Ostowari and Naik [21] and Tangler and Kocurek [22] were used. Representative results for a NACA 4412 operating at a Reynolds number of  $1 \times 10^6$  are shown in Fig. 8. From this merged set of analytical and experimental data, maps of sectional lift and drag coefficients across a range of angle of attack and Reynolds number were created. Sectional lift and drag coefficients for the BEM model

at a particular condition can then be obtained from these data using the MATLAB bi-linear interpolation function (Fig. 9).

## C. Operating Conditions

The BEM model was applied to three propeller geometries discussed previously. The performance of each propeller was modeled over a range of advance ratios and Reynolds numbers, the limits of which were selected from previous flight and wind tunnel testing of the propulsion system (summarized in Table 1). For this testing, the Reynolds number is defined based on blade diameter and the resultant blade-relative velocity evaluated at 70% of the blade radius. This radial position represents the approximate location of the average force acting on the blade. It should be noted that the BEM model uses the local chord to determine the Reynolds number for aerodynamic parameter estimation.

## IV. Experimental Testing

Thrust and power data for common hobby grade motor and propeller systems are typically highly dependent on the specific components tested [23]. Therefore, a successive buildup method is proposed to quantify the individual component efficiencies for the propeller and motor, along with the propulsion system thrust and torque coefficients. A test stand in a wind tunnel was used for measurement of the thrust and torque over a range of airspeeds and motor speeds in order to generate a map of propeller efficiency versus advance ratio. In addition to the thrust and torque data, engine RPM, motor voltage, and current were monitored. Figure 10 shows a schematic of the engine testing apparatus.

### A. Experimental Setup

The thrust and torque measurements were made using a Futek MBA500 with a thrust rating of  $222 \text{ N}$  ( $\pm 0.1 \text{ N}$ ) and a torque capacity of  $5.64 \text{ N} \cdot \text{m}$  ( $\pm 2.8 \times 10^{-3} \text{ N} \cdot \text{m}$ ). The maximum thrust

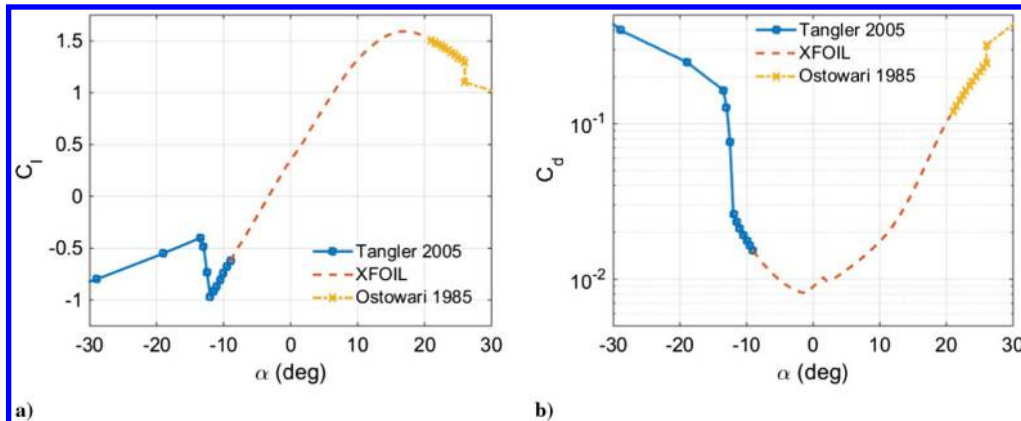


Fig. 8 Lift (a) and drag (b) coefficients for the NACA 4412 at  $Re = 1 \times 10^6$ , drawing on data from Ostowari and Naik [21] and Tangler and Kocurek [22].

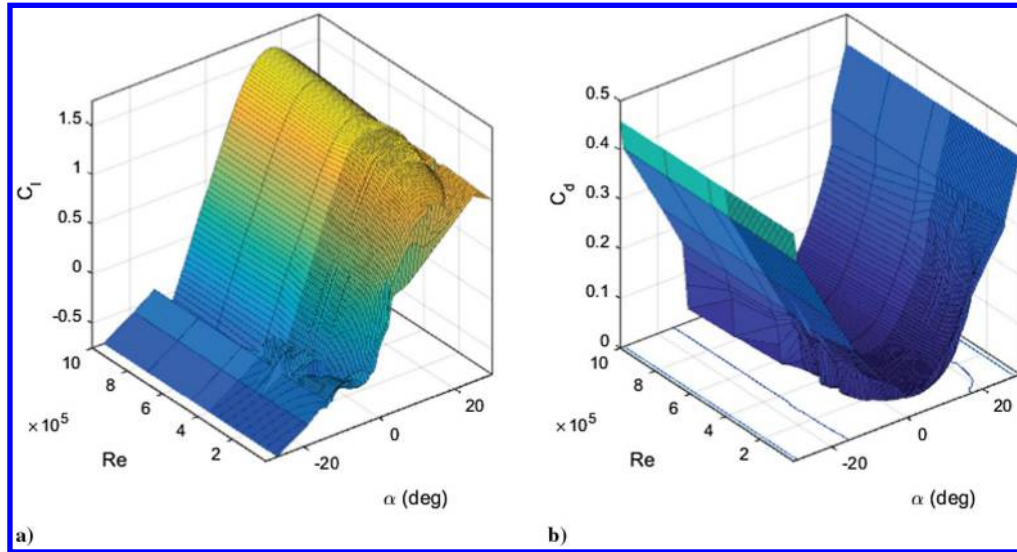


Fig. 9 Lift (a) and drag (b) coefficients versus angle of attack and Reynolds number for NACA 4412.

recorded was 16 N and the maximum moment was 0.27 N · m. Measurements of rotational speed were made based on the back EMF produced by the commuting motor. The back EMF signal contains a voltage spike each time the coils in the motor are energized. The back EMF signal was passed through a Schmitt trigger, which provided a square wave output proportional to the motor speed with six pulses per revolution. An inline Allegro ACS758 100-A current sensor allowed for measurement of the electrical power. A bank of six HP Proliant 406421-001 1300-W, 12-V server power supplies provided the electrical power necessary to run the motor. Each power supply was capable of providing 40 A and was placed in parallel to buffer the current output capability.

The wind tunnel is an open return type with a 22'' × 22'' test section and a maximum velocity of 65 m/s. The tunnel features a 3'' flow straightening honeycomb structure on the inlet, followed by three turbulence-reducing screens. Tunnel velocity was measured using two static rings, with one placed in the plenum after the turbulence screens, and the other immediately before the test section. Test section dynamic pressure was measured across the two static rings using an Omega PX2650 differential pressure transducer. The test section is sealed; therefore, the local static pressure was measured at both the upstream and downstream ends of the test section, in order to account for buoyancy effects. Test section static pressure was measured using two Omega PX2650 differential pressure transducers. The static temperature was measured near the test article using a K-type thermocouple and a National Instruments NI-9213 thermocouple amplifier. A model-following controller designed in LabVIEW controls the wind tunnel velocity. The controller allows for fast ramping and precise control over the test section velocity.

The motor revolution speed, current, voltage, torque, and thrust signals were sampled using a National Instruments NI-6009 data acquisition board. The DAQ gathers analog and digital information from all sensors at 10 kHz. The sampling rate was sufficiently higher than the vibrational modes of the thrust stand (2 kHz), which limited aliasing and allowed for adaptive filtering in the data reduction. The

motor was mounted directly to the load cell for force and torque measurement, and the motor/load cell assembly was positioned in the center of the test section on a faired mount. A vibration isolation mount held the motor and increased the natural resonant frequency of the motor/propeller combination beyond the upper RPM limit. The vibration mount made the calibration of the thrust and torque sensor more difficult by introducing elasticity into the system. However, the calibrations were repeatable over the course of the experimental campaign.

Testing of the propellers at a constant Reynolds number across a range of advance ratios requires a reduction of the propeller RPM while the tunnel speed is increased. For this testing, the Reynolds number is evaluated based on the resultant freestream and rotational velocity components, evaluated at 70% of the blade span. If the density and viscosity are treated as constants, the constant Reynolds number testing reduces to maintaining a constant resultant velocity evaluated at 70% of the blade span [formulated in Eq. (16), where induction factors are neglected]. The resulting variation in chord-based Reynolds number is shown in Fig. 11 for a blade-based Reynolds number of  $5 \times 10^5$ . Coordinated control of the tunnel/propeller combination for constant  $Re$  is complicated by the fact that the propeller induces significant flow in the tunnel. Furthermore, for the fixed-pitch propellers tested in this work, as the freestream velocity changes, the angular velocity of the propeller also changes (even when applied power is held constant). This is because of a decreased angle of attack at high advance ratios, resulting in a drag reduction. The drag reduction decreases the power required to drive the propeller, resulting in a higher rotational velocity [24].

$$n = \sqrt{\frac{V_l^2 - V_\infty^2}{(2\pi 0.7r)^2}}; \quad V_l = \frac{Re\mu}{\rho D} \quad (16)$$

For all of these reasons, careful real-time closed-loop control of the propeller speed and tunnel velocity must be done in order to maintain the desired Reynolds number. A standalone RPM and throttle controller, based on a microcontroller from Parallax Propeller, was integrated with tunnel speed control in LabVIEW for closed-loop control of the coupled test conditions. Using these devices, This setup allowed the propeller Reynolds number to be held constant within 3% of the desired set point over the full range of advance ratios.

## B. Wind Tunnel Correction Factors

Two correction factors were used to account for the influence of the wind tunnel on the performance of the system. The first accounts for the tunnel wall effects that can increase the static pressure in the propeller wake [25]. Following the work of Barlow et al. [25] and

Table 1 BEM model operational bounds

Parameter	Minimum	Maximum
$J$	0.01	1
$n$	4000 RPM	15,000 RPM
$V_\infty$	0.01 m/s	45 m/s
$Re$	$1 \times 10^5$	$1 \times 10^6$
$M$	0.16	0.6

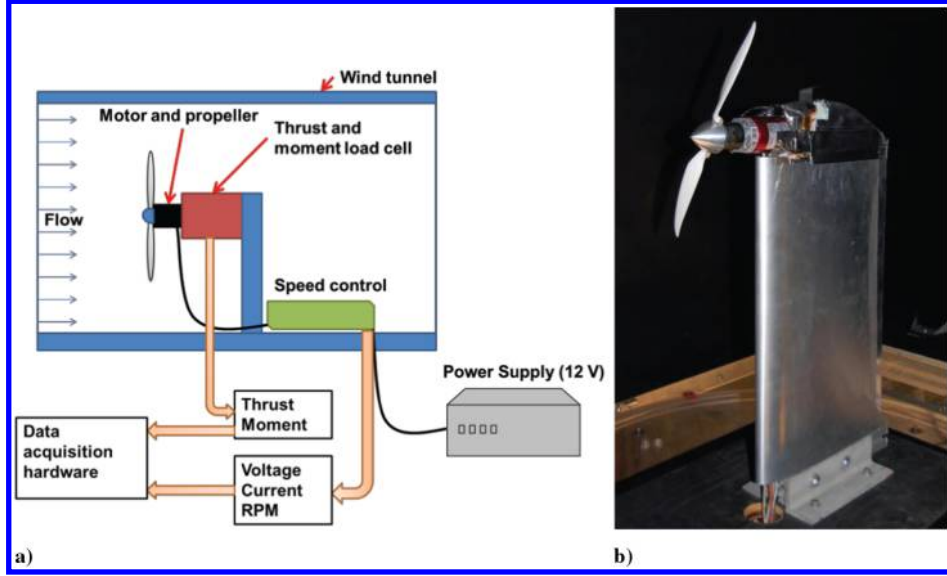


Fig. 10 Schematic of propulsion system test setup (a) and photograph of experimental test stand (b).

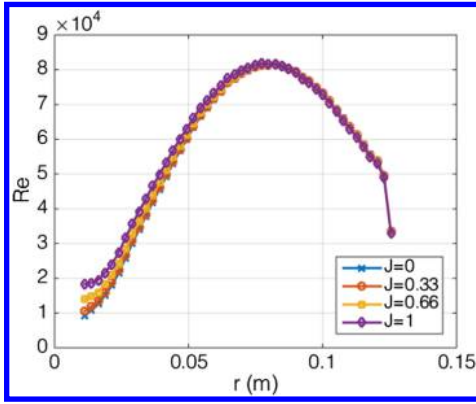


Fig. 11 Variation in chord-based Reynolds number during constant Reynolds testing at  $Re = 1 \times 10^5$  for different advance ratios.

Brandt and Selig [7], the following corrected velocity is used in place of the measured tunnel velocity:

$$\frac{V_{\infty, \text{corr}}}{V_{\infty}} = 1 - \frac{TA/qC}{2\sqrt{1 + 2(T/q)}} \quad (17)$$

The second correction addresses the local velocity increase caused by the presence of a 3D body in the wind tunnel (solid blockage). To correct the artificial increase in velocity, the method proposed by Brandt and Selig was used [7]. Briefly, the increase in velocity is related to the relative volume of the test piece and the overall wind tunnel geometry. The relationship for the relative increase in velocity is given by [25]:

$$\frac{V_{\infty, \text{corr}}}{V_{\infty}} = \frac{K\tau V}{A^{3/2}} \quad (18)$$

where  $K = 1.045$ ,  $\tau = 0.92$ , and the volume of the fairing ( $V$ ) is  $3.28 \times 10^{-3} \text{ m}^3$ .

## V. Results

This section compares the predictions generated using the BEM model and data gathered during experimental testing of the three propellers considered in this work. The first section details the full-power, high-RPM performance of the propeller via modeling and experimental results. Using these data, the effects of the three proposed corrections to the BEM are each illustrated separately. The

effects of varying the Reynolds number are then demonstrated and compared with experimental data gathered using the constant Reynolds testing method outlined previously. Finally, the complete system performance is detailed using measurements of the electrical efficiencies of the supporting propulsion hardware.

Uncertainty in the experimental data was estimated via a Monte Carlo simulation of the complete data acquisition and reduction process [26]. The resulting uncertainty varies with the particular experimental conditions (e.g., because of the quoted accuracy of the pressure transducers used for wind tunnel freestream velocity measurements, low-speed data points will have higher uncertainty). Thus, the following experimental data sets are presented with error bars on each data point that express the 95% confidence interval for advance ratio, thrust coefficient, torque coefficient, and propulsive efficiency.

### A. Full-Power Performance

#### 1. Thrust and Torque Coefficients

The initial set of data presented here is for the propeller operating at full power (fixed voltage) across a range of advance ratios. These experimental data and the corresponding BEM analytical prediction serve to quantify the uncertainty associated with the experimental data and to validate the model. Furthermore, full-power tests demonstrate the upper performance limit for each propeller and establish bounds for the mapping between  $\eta_{\text{propulsive}}$ ,  $J$ , and the Reynolds number.

For these initial validation tests at full power, the advance ratio was controlled by varying the test section velocity and the Reynolds number was not strictly controlled. In this type of testing, the blade Reynolds number will vary on the order of 10% as flow conditions change. This is because an increase in freestream velocity reduces the blade angle of attack, thus reducing the induced drag and the motor torque requirement (for a fixed-pitch propeller). The reduction in motor torque required, while full power is applied, allows the motor to rotate at a higher speed. An increase in rotational speed results in changes to the local Reynolds number and tip Mach number in a parabolic fashion. The Reynolds number used for the BEM model prediction was selected as the average propeller Reynolds number encountered during the full-power testing.

Figure 12 shows the BEM model results for the predicted and measured thrust and torque coefficients. The overall trend of the BEM model data matches the experimental data very well, with any differences between the two being less than the experimental uncertainty for all three propellers studied in this work. The decrease in the experimental  $C_T$  uncertainty at high advance ratios is caused primarily by the increase in RPM. The uncertainties associated with density and diameter are small and do not change appreciably with

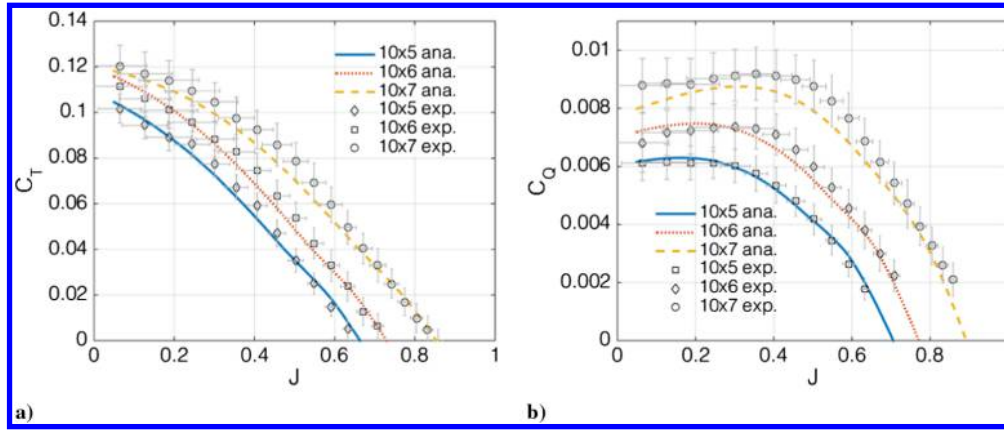


Fig. 12 Analytic and experimental thrust (a) and torque (b) coefficients for the APC  $10 \times 5E$ ,  $10 \times 6E$ , and  $10 \times 7E$  at  $Re \approx 1.5 \times 10^6$ . Error bars depict uncertainty in experimental data.

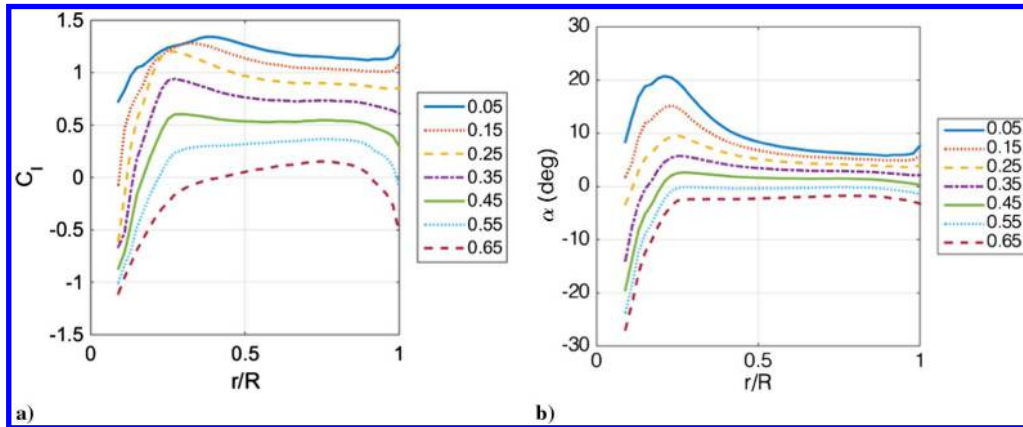


Fig. 13 Spanwise  $C_l$  (a) and angle of attack (b) variation at different advance ratios for APC  $10 \times 5E$  at  $Re \approx 1.5 \times 10^6$ .

increasing  $J$ . The variation in  $J$  at low advance ratios is because primarily of the dominant influence of the static and dynamic pressure uncertainties. As the advance ratio increases, this effect is somewhat offset by the increasing rotational velocity.

The accuracy of the BEM model thrust prediction is largely dependent on the fidelity of the local lift coefficient estimates. Within the advance ratios considered, the lift coefficient varies appreciably from  $-1$  to  $1.25$  with an angle-of-attack variation between  $-30$  and  $25$  deg, as shown in Fig. 13. The variation in angle of attack and lift coefficient is much more significant near the hub, which indicates that this region of the blade could drive the accuracy of the model under certain conditions. The data presented compare favorably with Brandt and Selig's investigation of the APC thin electric  $10 \times 5E$  and

$10 \times 7E$  at lower angular velocities (Fig. 14) [27]. This comparison is based on experimental testing performed at similar operating conditions to those outlined by Brandt and Selig and involved holding the propeller RPM constant as the freestream velocity was increased.

The difference between experimental and BEM torque results (Fig. 12) at low advance ratios for the APC  $10 \times 7E$  is likely because of the angle of attack being beyond stall over the majority of the blade. In this condition, the predicted torque is sensitive to the magnitude of the drag coefficient, which increases parabolically with angle of attack. At low advance ratios, the inboard sections of the blade are stalled as shown in Fig. 15. These stalled regions largely govern the required torque. As the advance ratio is increased, the

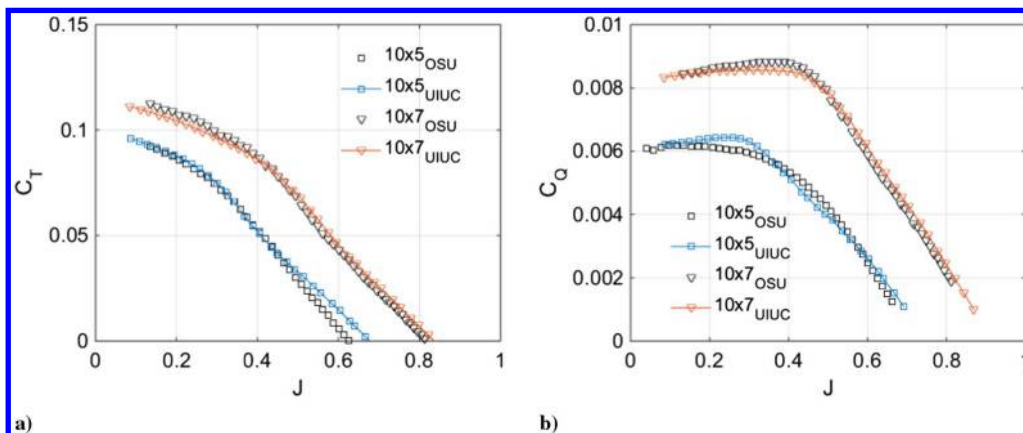


Fig. 14 Comparison of thrust coefficient (a) and torque coefficient (b) data between the current work (The Ohio State University) and independently acquired data from Brandt and Selig (University of Illinois at Urbana-Champaign [27]) for APC  $10 \times 5E$  and  $10 \times 7E$ .



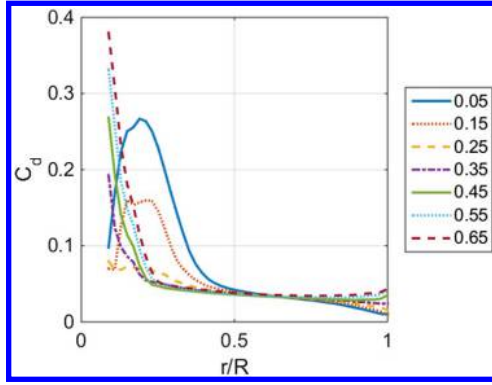


Fig. 15  $C_d$  versus spanwise location for different advance ratios for APC  $10 \times 5E$  at  $Re \approx 1.5 \times 10^6$ .

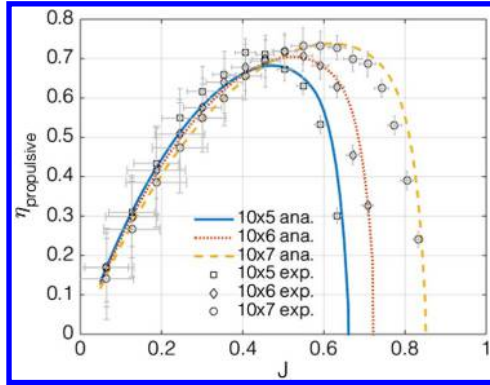


Fig. 16 Analytic and experimental propulsive efficiency for the APC  $10 \times 5E$ ,  $10 \times 6E$ , and  $10 \times 7E$  at  $Re \approx 1.5 \times 10^6$ . Error bars depict uncertainty in experimental data.

torque required is relatively constant until the local angle of attack drops below the stall angle. Below the stall angle, the required torque drops dramatically and the blade efficiency will increase.

## 2. Propulsive Efficiency

Figure 16 shows the BEM model predictions and experimental measurements of the propulsive efficiency for the three propellers considered in this work. The experimental measurements closely match the predicted performance provided by the BEM model. The uncertainty in propulsive efficiency at low advance ratios is dictated primarily by the uncertainty in the airspeed. As the advance ratio increases, the ratio of uncertainty in the thrust and moment is relatively constant. Therefore, increasing RPM at higher advance ratios decreases the total uncertainty.

The design pitch of the propeller can be determined by finding the upper advance ratio limit at which the thrust and efficiency are zero. At this point, the geometric pitch (reported by the manufacturer) is equal to the advance ratio multiplied by the diameter of the propeller. Table 2 summarizes the pitch determined from BEM theory and from experimental data, along with the pitch specified by the propeller manufacturer. These results show that the model and experimental data are in close agreement with one another. The manufacturer's reported pitch for all three propellers is lower than the experimental and analytic estimates, which is consistent with other investigations of similar propellers [7,8]. The performance variation is more

dramatic when comparing propellers of the same diameter and pitch from different manufacturers [7,8,23].

## B. BEM Model Correction Factors

Having established the fidelity of the BEM model to the experimental data, the significance of the contribution from each correction factor will be evaluated in turn. The correction factors applied to the BEM model are a tip loss model, Mach correction, and quasi-3D spanwise flow correction. To demonstrate the effect of each correction individually, the BEM model was run with each switched off in isolation. A comparison between the BEM models with no corrections is also presented for reference. The resulting model data are then shown relative to the experimental data, with thrust and torque data serving as the basis for comparison.

### 1. No Correction Factors

For comparative purposes, the BEM model is presented with no corrections, as shown in Fig. 17. The fully corrected BEM model results and experimental data are also shown. The basic trend of the uncorrected model is in reasonable agreement with the experimental data at moderate advance ratios, but there is a significant offset across all conditions. Furthermore, at low advance ratios, the model fails to capture the trend present in the experimental data. Thus, the uncorrected BEM model is generally insufficient for predicting the propeller performance.

### 2. Tip Loss Correction

The Prandtl tip loss correction model forces the lift to approach zero at radial locations approaching the blade tip, in an effort to capture the pressure equalization occurring near the tip of finite lifting surfaces. Tip losses are most pronounced at low advance ratios where the blade is highly loaded and, if not stalled, operating with high local lift and drag coefficients. The effect of neglecting the tip loss model is shown in Fig. 18. In this figure, the largest differences between experimental data and the BEM model occur below advance ratios of approximately 0.5. Below  $J = 0.5$ , the higher lift and drag near the tip (without tip-loss correction) results in higher predicted torque and thrust.

### 3. Mach Correction

The Mach correction increases the lift curve slope as a function of local Mach number. This effect is pronounced when high lift coefficients and high rotation rates are simultaneously present. These conditions occur at low advance ratios as evidenced in Fig. 19. The BEM model without Mach correction underpredicts the thrust at low advance ratios, particularly for the more highly loaded  $10 \times 7E$  propeller. The lower lift coefficients associated with the BEM model without Mach correction result in lower drag, and underpredicted power (torque) to drive the propeller.

### 4. Three-Dimensional Flow Correction

The 3D correction modifies the local lift coefficient parabolically in the spanwise direction. The correction concentrates the largest effect near the tip region. In this region, the local lift coefficient is typically lower than the lift coefficient from potential flow theory, thus providing an amplification to the normal force coefficient. At low advance ratios this increases the lift and drag components. This translates to an increase in thrust and torque. As the advance ratio increases, the ratio of the rotational velocity to the local velocity decreases, thus diminishing the effect of the correction. The effect

Table 2 Analytic advance ratio

Propeller	Published pitch (inches)	Analytic pitch (inches)	Experimental pitch (inches)	Percent difference Pub./Ana.	Percent difference Pub./Exp.	Percent difference Ana./Exp.
APC $10 \times 5E$	5	6.4	6.5	28	30	1.5
APC $10 \times 6E$	6	7.2	7.4	20	23	2.7
APC $10 \times 7E$	7	7.9	8.2	13	17	3.8

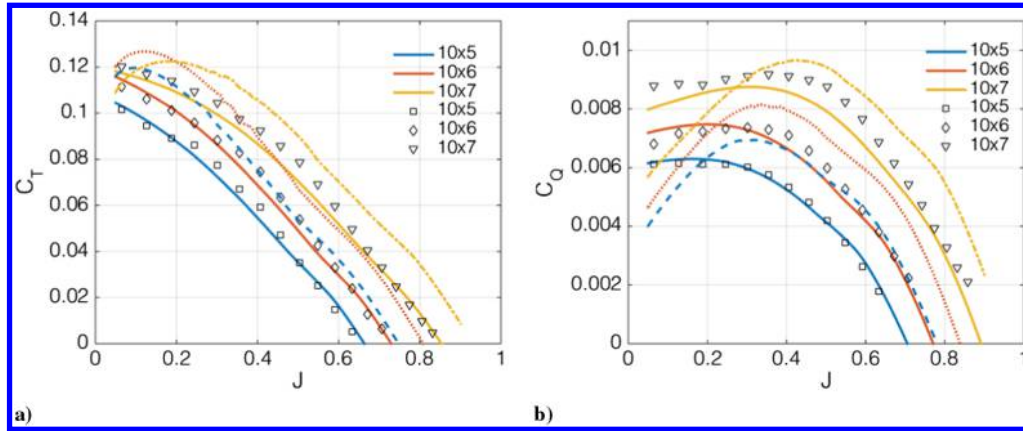


Fig. 17 Thrust coefficient (a) and torque coefficient (b) for BEM model results with no corrections (dashed lines). Fully corrected BEM model (solid lines) and experimental results (symbols) shown for comparison at  $Re \approx 1.5 \times 10^6$ .

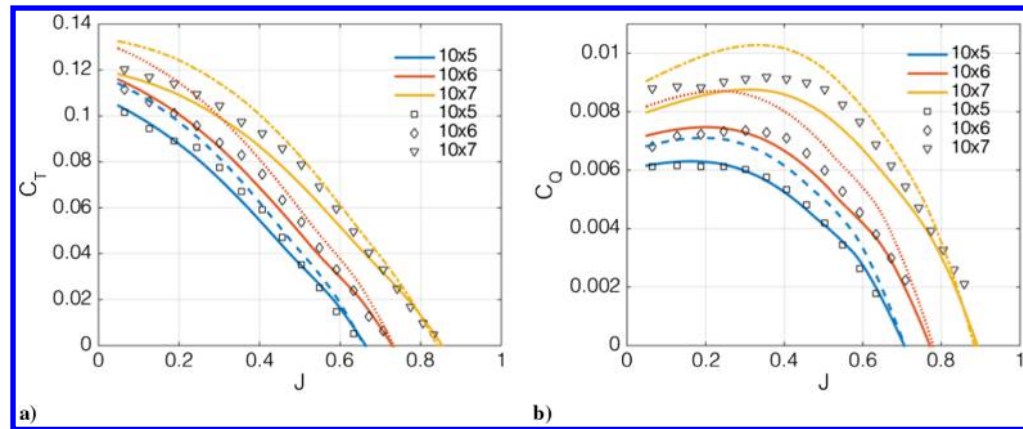


Fig. 18 Thrust coefficient (a) and torque coefficient (b) for BEM model predictions without tip loss correction (dashed lines) and fully corrected BEM model (solid lines). Experimental results (symbols) shown for  $Re \approx 1.5 \times 10^6$ .

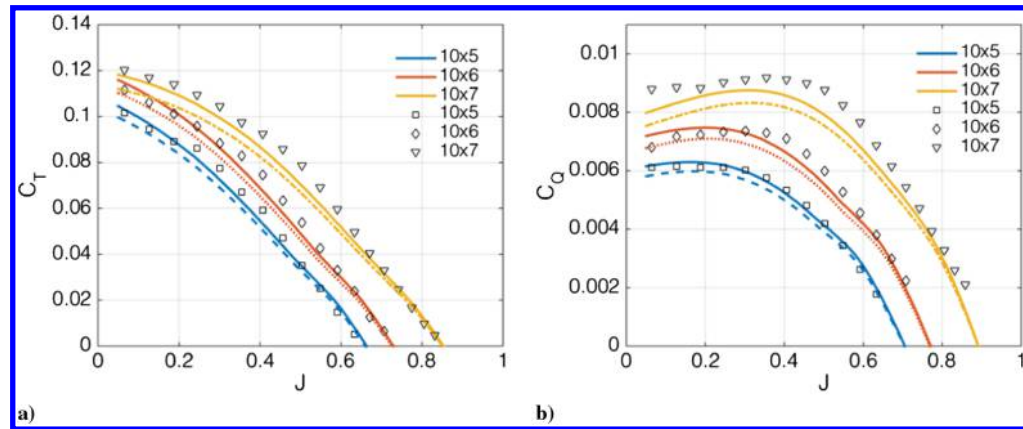


Fig. 19 Thrust coefficient (a) and torque coefficient (b) for BEM model predictions without Mach correction (dashed lines) and fully corrected BEM model (solid lines). Experimental results (symbols) shown for  $Re \approx 1.5 \times 10^6$ .

increases with the difference between the potential flow lift coefficient and the local 2D lift coefficient. For a highly loaded blade, such as the  $10 \times 7$ , the reduction in thrust and torque (shown in Fig. 20) at low advance ratios caused by omitting the correction is clearly visible. The advance ratios over which the correction is effective are complicated by the inclusion of the local velocity component. The BEM model approximates the axial and radial induction factors iteratively, making the analytic application of the correction difficult.

### C. Reynolds Number Effects

The BEM model was used to predict the performance of propellers at varying Reynolds numbers. The inclusion of the BEM model is

critical to this effort as the local variation in spanwise Reynolds number is appreciable on the scale of the propellers tested, and is in the range where viscous effects become significant. The effects of Reynolds number have been explored by others for sUAS propellers [7,14]. Both Deters et al. and Brandt and Selig presented experimental data for similar propellers tested at a constant RPM, showing a reduction in propulsive efficiency at lower chord-based Reynolds number. The present work seeks to build on these studies by tightly controlling the propeller diameter-based Reynolds number over the range of positive thrust advance ratios. The predictions generated by the BEM model are then compared with wind tunnel measurements using the same experimental apparatus as the full-power tests. For the experimental data presented in this subsection,

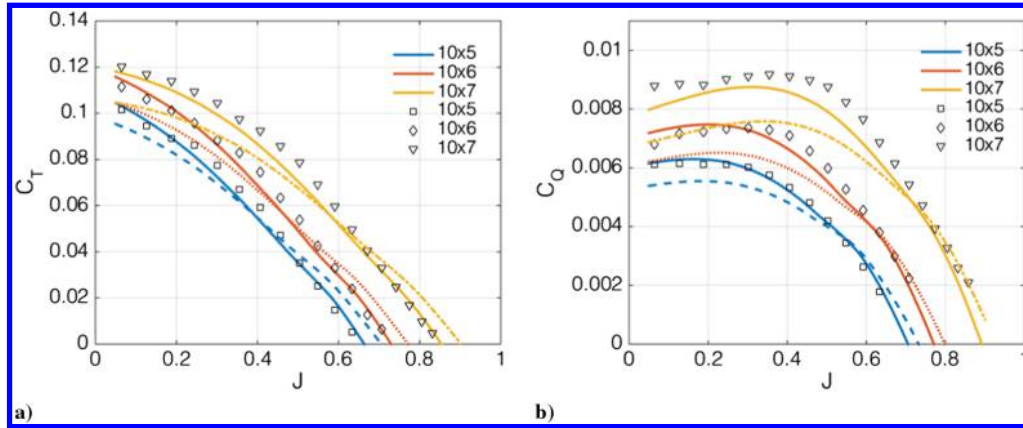


Fig. 20 Thrust coefficient (a) and torque coefficient (b) for BEM model predictions without 3D correction (dashed lines) and fully corrected BEM model (solid lines). Experimental results (symbols) shown for  $Re \approx 1.5 \times 10^6$ .

the diameter-based Reynolds number was tightly controlled via the closed-loop testing method described in the experimental setup. In the current work, the Reynolds number for the experimental data is defined based on the propeller diameter and blade-relative velocity occurring at 70% of the span. The same operating conditions are applied to the BEM model results, where sectional aerodynamic coefficients were determined based on local Reynolds number.

Figure 21 shows the variation in propulsive efficiency for the APC  $10 \times 7E$  at different Reynolds numbers. For low advance ratios, the overall trend is unaffected by the change in Reynolds number. At high advance ratios, however, there is a significant impact of Reynolds number. Efficiency curves for fixed-pitch propellers are characterized by a rapid drop in efficiency near the maximum advance ratio. As seen in Fig. 21, the rapid drop in propeller efficiency occurs at lower advance ratios when the Reynolds number is decreased. This is because the NACA 4412 airfoil section used on these propellers experiences a dramatic increase in drag and decrease in lift over a relatively small decrease in Reynolds number (Fig. 22). It is important to note that, in the current modeling environment, the Reynolds number is evaluated on the quasi-2D BEM model before the 3D correction is applied (a one-way coupling of viscous effects). However, the spanwise variation in local velocity and local Reynolds effects are expected to be tightly coupled (two way). Accurate modeling of these coupled viscous effects would require much higher fidelity modeling, which would be prohibitively complex and expensive for the current purposes. Despite the low fidelity of this viscous modeling approach, the BEM theoretical curves still show good agreement with the experimental data and clearly show the appropriate changes in the propeller efficiency curves as Reynolds number changes.

The performance difference at the three representative Reynolds numbers can be explained by a spanwise variation in aerodynamic characteristics. For the constant Reynolds number tests, the ratio of

the freestream velocity and rotational velocity remains constant. Therefore, the angle of attack is relatively constant between Reynolds cases. Subtle variations are present because of the induced velocity components that change as a function of the local lift and drag coefficients. Figure 23 shows the BEM-model-predicted angle of attack for the three Reynolds number test cases at the same advance ratio. Although the angle of attack changes very little with Reynolds number, the lift and drag coefficients vary significantly, as shown in Fig. 24.

Figure 25 shows the predicted variation in performance over a range of Reynolds numbers for the three propellers tested in this work. From this figure it is evident that the effect of changing Reynolds numbers is equivalent in some cases to operating with a different propeller pitch. It is clear from this plot that incorporating the Reynolds number into the basic BEM model is of first-order importance for propellers on this physical scale. In some cases,

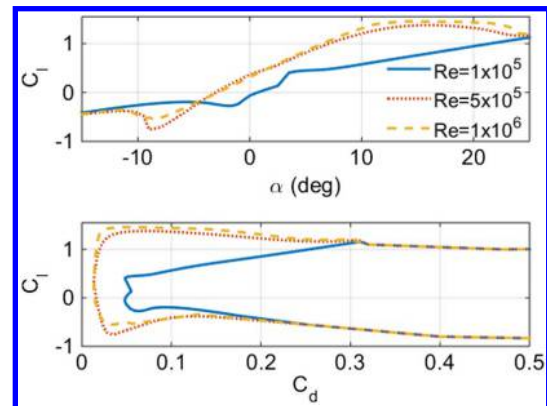


Fig. 22 Lift curve and drag polar for the NACA 4412 at different Reynolds numbers, generated using XFOIL [20].

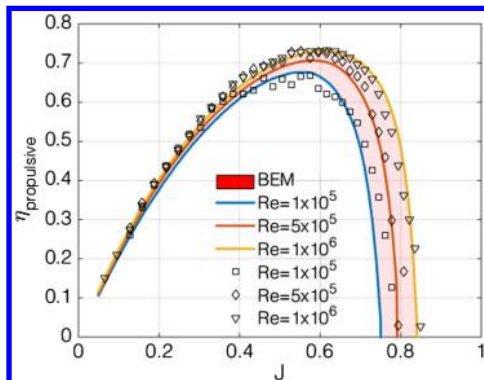


Fig. 21 BEM model (lines and shaded region) and experimental (symbols) propulsive efficiency for the APC  $10 \times 7E$  at varying Reynolds numbers.

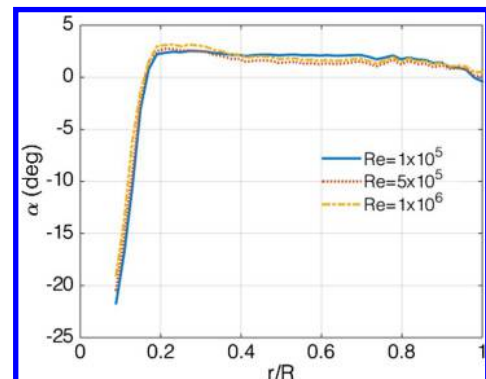


Fig. 23 Spanwise angle-of-attack variation for different Reynolds numbers, APC  $10 \times 7E$  at  $J = 0.55$ .



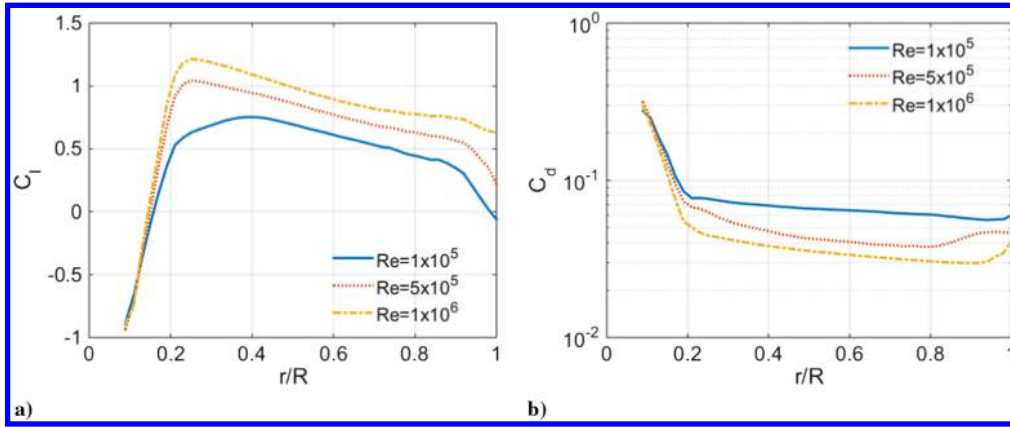


Fig. 24 Spanwise  $C_l$  (a) and  $C_d$  (b) for different Reynolds numbers, APC  $10 \times 7E$  at  $J = 0.55$ .

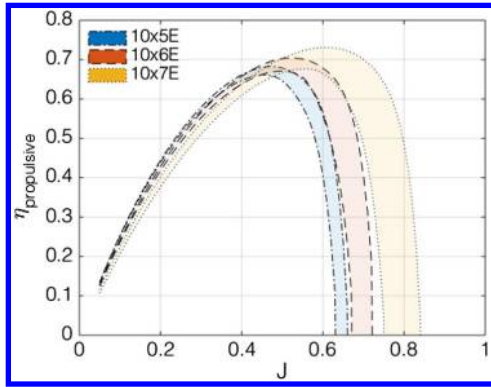


Fig. 25 Variation in performance for the APC  $10 \times 5E$ ,  $10 \times 6E$ , and  $10 \times 7E$  operating with Reynolds numbers between  $1 \times 10^5$  and  $1 \times 10^6$ .

incorporation of Reynolds-varying aerodynamic parameters has a larger effect on the predicted results than the three other correction factors combined (Prandtl tip loss, compressibility, and 3D corrections). Incorporation of Reynolds effects in the BEM is increasingly important at low rotation rates where the local variation in lift and drag is much larger. At higher Reynolds numbers, the performance shows a much smaller overall variation as the change in aerodynamic parameters is not as severe.

#### D. System Efficiency

The final characterized component is the electrical efficiency of the power system. The electrical efficiency term allows for the correlation between measured electrical power and propulsive efficiency. The electrical efficiency is given as the ratio of motor and applied electrical power. This encompasses the power delivery

system and motor mechanical efficiency. Typical efficiencies for the power system components range from 70 to 90% and depend on operating temperature and electrical load [8]. The battery represents another efficiency term, but as the power in this work is measured downstream of the battery terminals, it does not impact the overall measured system efficiency.

Figure 26 shows the electrical efficiency for the three representative propellers tested at full power. This figure shows an appreciable and nonlinear variation in electrical efficiency parameterized by advance ratio. To use these data in a predictive model, a surface fit is necessary. From Fig. 26, approaching the full-power design pitch, the electrical efficiency decreases by up to 10%. The speed controller efficiency decreases at high angular speeds and low power output, likely because of internal switching inefficiencies and timing delays. The variation in electrical efficiency versus Reynolds number shows similar trends. At low Reynolds numbers, the efficiency decreases as the advance ratio approaches the design pitch. As the Reynolds number increases, the efficiency at low advance ratios plateaus before sharply decreasing close to the design pitch. The trend is monotonic and similar between propellers operating at the same Reynolds number. The similarity in trends allows for the generation of a parameterized surface fit. Figure 27 shows an example of the surface fit for the electrical efficiency versus advance ratio. From this plot, the monotonic trend is fit by a third-order polynomial surface. The resulting fit has an adjusted  $R$ -squared value of 0.89. The electrical efficiency is combined with the propulsive efficiency to determine the overall system efficiency as a function of Reynolds number and advance ratio. The surface fit, shown in Fig. 27, allows for inflight estimation of the power available and thrust based on measured airspeed, electrical power, and propeller rotation speed. The parameterized surface fit is a critical component necessary for future vehicle performance estimation. This surface fit could have a significant overall impact on the range and/or endurance of an electric-powered sUAS.

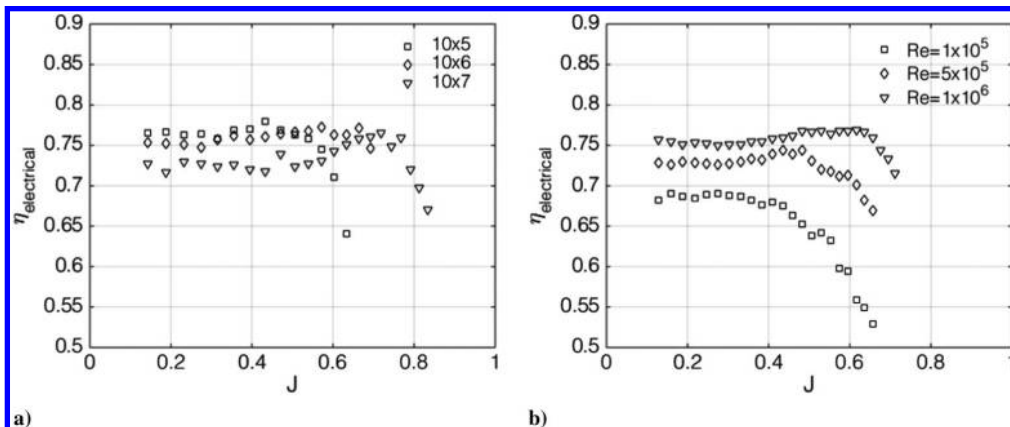


Fig. 26 Electrical efficiency for the APC  $10 \times 5E$ ,  $10 \times 6E$ , and  $10 \times 7E$  tested at full power (a). Electrical efficiency for the APC  $10 \times 6E$  tested at different Reynolds numbers (b).



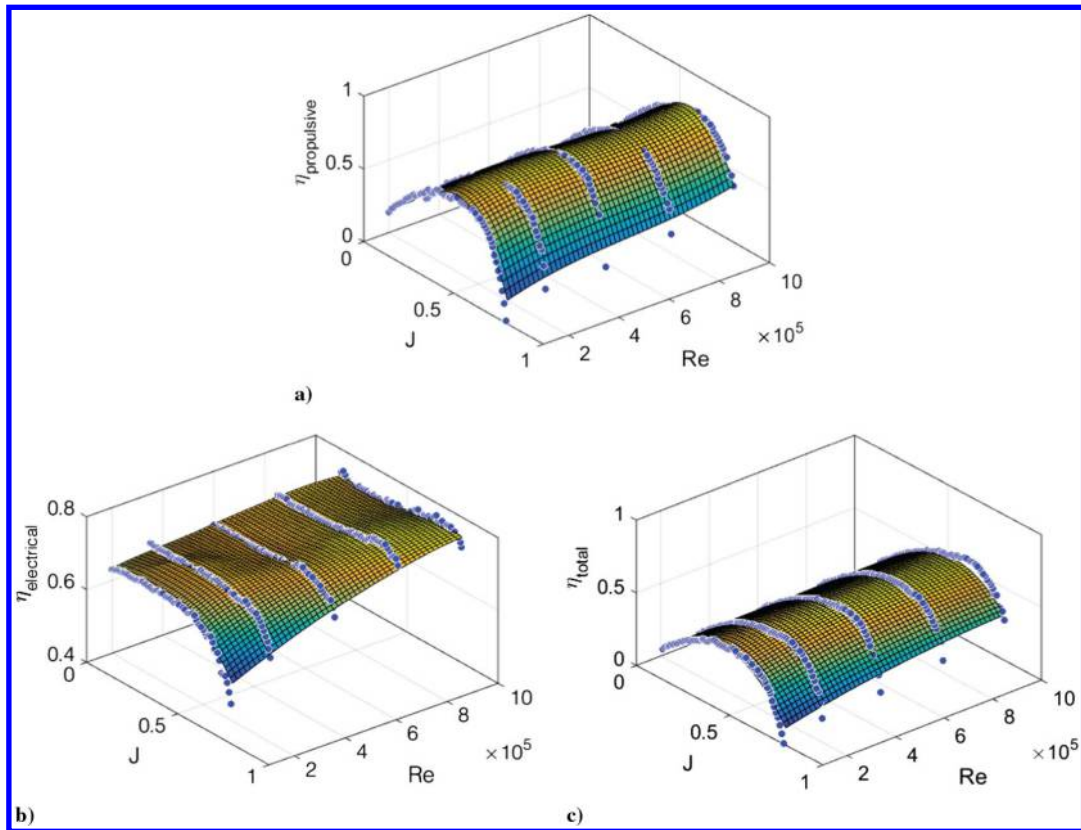


Fig. 27 Surface fit of propulsive efficiency versus  $Re$  and  $J$  (a), electrical efficiency versus  $Re$  and  $J$  (b), and the total system efficiency (c) versus  $Re$  and  $J$  for the APC  $10 \times 7E$ .

## VI. Conclusions

A blade element momentum (BEM) model is presented and used for performance predictions on sUAS propellers. Several corrections were proposed to the BEM model to capture features unique to the rotational flow around finite low-Reynolds-number propellers. Namely, the use of an XFOIL-generated aerodynamic database, tip loss corrections, Mach corrections, and the incorporation of spanwise flow components were added to the model. For the specific propeller geometries considered in this work, the BEM model predictions follow the general trends expected for fixed pitch propellers.

The BEM model was validated by a series of wind tunnel tests. From these tests, favorable comparisons between the predicted and measured theoretical pitch were noted. Full-power testing yielded results similar to those published in previous studies of small-scale propellers. A novel constant-Reynolds-number test was presented to demonstrate the effects of scale on the propulsive efficiency. The favorable comparison between experimental- and model-based performance metrics such as propulsive efficiency and thrust/power coefficients point toward the importance of incorporating Reynolds dependency in the analysis of small-scale propulsion systems. The methodology for determining the performance of the remaining individual propulsion components such as the motor and electronic speed controller was presented. Using these estimates, the system efficiency neglecting the battery was determined. These estimates allow for a direct correlation between measured electrical power, advance ratio, and propulsive efficiency. From the propulsive efficiency, the thrust and power available can be estimated.

The BEM model presented and validated here is highly useful for propeller design for sUAS, particularly because the operating Reynolds numbers of these vehicles are low enough where viscous effects are of first-order importance. Furthermore, the overall power available model for the sUAS propulsion system enables high-fidelity vehicle performance estimates for sUAS and inflight determination of vehicle performance for flight testing and routine operations.

## References

- [1] Madsen, H. A., Mikkelsen, R., and Øye, S., "A Detailed Investigation of the Blade Element Momentum (BEM) Model Based on Analytical and Numerical Results and Proposal for Modifications of the BEM Model," *Journal of Physics: Conference Series*, Vol. 75, No. 012016, 2007, pp. 1–11. doi:10.1088/1742-6596/75/1/012016
- [2] Merrill, R. S., "Nonlinear Aerodynamic Corrections to Blade Element Momentum Model with Validation Experiments," M.S. Thesis, Mechanical and Aerospace Engineering, All Graduate Plan B and Other Reports, Utah State Univ., Logan, UT, 2011, <http://digitalcommons.usu.edu/gradreports/67> [accessed Jan. 2014].
- [3] Snel, H., Houwink, R., and Bosschers, J., "Sectional Prediction of Lift Coefficients on Rotating Wind Turbine Blades in Stall," Energyresearch Centre of the Netherlands (ECN), ECN-C-93-052, Petten, The Netherlands, Dec. 1994, <ftp://ftp.ecn.nl/pub/www/library/report/1993/c93052.pdf> [accessed Jan. 2014].
- [4] Uhlig, D. V., and Selig, M. S., "Post Stall Propeller Behavior at Low Reynolds Numbers," *46th AIAA Aerospace Sciences Meeting and Exhibit*, AIAA Paper 2008-0407, Jan. 2008. doi:10.2514/6.2008-407
- [5] Barnitsas, M. M., Ray, D., and Kinley, P., " $K_T$ ,  $K_Q$  and Efficiency Curves for the Wageningen B-Series Propellers," Dept. of Naval Architecture and Marine Engineering, College of Engineering, The Univ. of Michigan, Rept. 237, Ann Arbor, MI, May 1981, <http://hdl.handle.net/2027.42/3557> [accessed Jan. 2014].
- [6] Ol, M., Zeune, C., and Logan, M., "Analytical-Experimental Comparison for Small Electric Unmanned Air Vehicle Propellers," *26th AIAA Applied Aerodynamics Conference*, AIAA Paper 2008-7345, Aug. 2008, pp. 18–21. doi:10.2514/6.2008-7345
- [7] Brandt, J. B., and Selig, M. S., "Propeller Performance Data at Low Reynolds Numbers," *49th AIAA Aerospace Sciences Meeting Including the New Horizons Forum and Aerospace Exposition*, AIAA Paper 2011-1255, Jan. 2011. doi:10.2514/6.2011-1255
- [8] Brezina, A. J., and Thomas, S. K., "Measurement of Static and Dynamic Performance Characteristics of Electric Propulsion Systems," *51st AIAA Aerospace Sciences Meeting Including the New Horizons Forum and*

- Aerospace Exposition*, AIAA Paper 2013-0500, Jan. 2013.  
doi:10.2514/6.2013-500
- [9] Gamble, D. E., and Arena, A., "Automated Dynamic Propeller Testing at Low Reynolds Numbers," *48th AIAA Aerospace Sciences Meeting Including the New Horizons Forum and Aerospace Exposition*, AIAA Paper 2010-0853, Jan. 2010.  
doi:10.2514/6.2010-853
- [10] Merchant, M., and Miller, S., "Propeller Performance Measurements for Low Reynolds Number UAV Applications," *44th AIAA Aerospace Sciences Meeting and Exhibit*, AIAA Paper 2006-1127, Jan. 2006.  
doi:10.2514/6.2006-1127
- [11] Shyy, W., Lian, Y., and Tang, J., *Aerodynamics of Low Reynolds Number Flyers*, Cambridge Univ. Press, Cambridge, U.K., 2008, pp. 28–76.  
doi:10.1017/CBO9780511551154
- [12] Kothari, A. P., and Anderson, J. D., "Low Reynolds Number Effects on Subsonic Compressibility Corrections," *Journal of Aircraft*, Vol. 24, No. 8, Aug. 1987, pp. 567–568.  
doi:10.2514/3.45477
- [13] Hoerner, S. F., and Borst, H. V., *Fluid-Dynamic Lift: Practical Information on Aerodynamic and Hydrodynamic Lift*, Hoerner Fluid Dynamics, Bakersfield, CA, 1992, pp. 2.1–2.24.
- [14] Deters, R. W., Ananda, G., and Selig, M. S., "Reynolds Number Effects on the Performance of Small-Scale Propellers," *AIAA Aviation, 32nd AIAA Applied Aerodynamics Conference*, AIAA Paper 2014-2151, June 2014.  
doi:10.2514/6.2014-2151
- [15] Leishman, J. G., *Principles of Helicopter Aerodynamics*, 2nd ed., Cambridge Univ. Press, Cambridge, U.K., 2006, pp. 115–167.
- [16] Hansen, M. O. L., *Aerodynamics of Wind Turbines: Rotors, Loads and Structure*, James and James Science Publ., London, 2000, pp. 48–59.
- [17] Shen, W. Z., Mikkelsen, R., and Sørensen, J. N., "Tip Loss Corrections for Wind Turbine Computations," *Wind Energy*, Vol. 8, No. 4, 2005, pp. 457–475.  
doi:10.1002/(ISSN)1099-1824
- [18] Lindenburg, C., "Investigation into Rotor Blade Aerodynamics," Energyresearch Centre of the Netherlands (ECN), ECN-C-03-025, Petten, The Netherlands, July 2003, <ftp://ftp.ecn.nl/pub/www/library/report/2003/c03025.pdf> [accessed Jan. 2014].
- [19] Liu, S., and Janajreh, I., "Development and Application of an Improved Blade Element Momentum Method Model on Horizontal Axis Wind Turbines," *International Journal of Energy and Environmental Engineering*, Vol. 3, No. 1, Dec. 2012, pp. 1–10.  
doi:10.1186/2251-6832-3-30
- [20] Drela, M., "XFOIL: An Analysis and Design System for Low Reynolds Number Airfoils," *Low Reynolds Number Aerodynamics*, edited by Mueller, T. J., Vol. 54, Lecture Notes in Engineering, Springer, Berlin, 1989, pp. 1–12.  
doi:10.1007/978-3-642-84010-4\_1
- [21] Ostowari, C., and Naik, D., "Post-Stall Wind Tunnel Data for NACA 44xx Series Airfoil Sections," Solar Energy Research Institute, SERI STR-217-2559, Golden, CO, Jan. 1985.  
doi:10.2172/5791328
- [22] Tangler, J., and Kocurek, J. D., "Wind Turbine Post-Stall Airfoil Performance Characteristics Guidelines for Blade-Element Momentum Methods," *43rd AIAA Aerospace Sciences Meeting and Exhibit*, AIAA Paper 2005-0591, Jan. 2005.  
doi:10.2514/6.2005-591
- [23] Corrigan, E. K., and Altman, A., "Survey of Small Unmanned Aerial Vehicle Electric Propulsion Systems," *46th AIAA Aerospace Sciences Meeting*, AIAA Paper 2008-0179, Jan. 2008.  
doi:10.2514/6.2008-179
- [24] Sequeira, C., Willis, D., and Peraire, J., "Comparing Aerodynamic Models for Numerical Simulation of Dynamics and Control of Aircraft," *44th AIAA Aerospace Sciences Meeting and Exhibit*, AIAA Paper 2006-1254, Jan. 2006.  
doi:10.2514/6.2006-1254
- [25] Barlow, J. B., Rae, W. H. J., and Pope, A., *Low-Speed Wind Tunnel Testing*, 3rd ed., Wiley, New York, 1999, pp. 344–374.
- [26] Coleman, H., and Steele, G. W., *Experimentation and Uncertainty Analysis for Engineers*, 2nd ed., Wiley, Hoboken, NJ, April 2008, pp. 47–79.
- [27] Brandt, J. B., "Small-Scale Propeller Performance at Low Speeds," M.S. Thesis, Dept. of Aerospace Engineering, Univ. of Illinois at Urbana-Champaign, Champaign, IL, 2005.

**This article has been cited by:**

1. Matthew McCrink, mccrink.2@osu.edu Ohio State University; James W. Gregory, gregory.234@osu.edu Ohio State University Range and Endurance Estimation for Low-Re Electric UAS . [[Citation](#)] [[PDF](#)] [[PDF Plus](#)]